Supplementary Information for

Realization of Kagome Kondo lattice

Boqin Song, Yuyang Xie, Wei-Jian Li, Hui Liu, Jing Chen, Shangjie Tian, Xing Zhang, Qinghong Wang, Xintong Li, Hechang Lei, Qinghua Zhang, Jian-gang Guo, Lin Zhao*, Shun-Li Yu*, Xingjiang Zhou, Xiaolong Chen*, Tianping Ying*

*Corresponding author. Email: ying@iphy.ac.cn (T. Y.); lzhao@iphy.ac.cn (L. Z.); slyu@nju.edu.cn (S. Y.); xlchen@iphy.ac.cn (X. C.)

Supplementary Note 1: Ultra-low carrier density

The fitting of the Hall coefficient R_H, as shown in Supplementary Fig. 4a, b. The Hall resistance R_{xy} below 280 K exhibits good linearity at most temperature, which can be fit using single-band model across all temperatures. However, this approach is questionable for the metallic behavior observed above T_F , as it would require an unrealistic decrease of the scattering rate. Given the absence of a phase transition, the two orders of magnitude variation in carrier concentration cannot be explained by temperature-dependent scattering from lattice, impurities, itinerant moments, or local moments at such high temperatures. This suggests that the single-band model is insufficient to fully capture our observations.

A more plausible explanation involves the presence of multiple carrier types, which can also lead to a linear R_{xy}, a possibility we initially overlooked. One scenario is that holes become localized as the temperature decreases, causing a significant change in R_H. While multiple carriers typically result in a nonlinear Hall response at high temperatures, our previous R_{xy} measurements above 280 K are too noisy to detect this due to the negligible Hall signal. To address this, we fabricated thinner flake samples (thinner than bulk but thicker than those exhibiting magnetic order) to enhance the Hall signal while still representing bulk behavior. As shown in Supplementary Fig. 4c, d, the field-dependent R_{xy} and extracted R_H from these samples are consistent with the bulk data, except for a sign change in R_H at 300 K. Notably, a nonlinear Hall response is clearly observed above 280 K, indicating a sign change in the dominant charge carriers.

We emphasize that our conclusion of ultra-low density at low temperature remains valid, as the linear Hall response cannot be fitted by a two-carrier model (since the R_H (B) term is magnetic field independent). However, we can still use the single-band model at the low temperatures to estimate the electron density, which is on the order of 10^{19} cm^{-3}. For the high temperature region, R_H remains valuable as it reflects a drastic change, regardless of the fitting model.

Supplementary Note 2: Magnetic moment and electron filling of Cr

By fitting the Curie-Weiss law of the bulk sample as Supplementary Fig. 5, we estimate the magnetic moment of chromium to be 1.76 μ_B/Cr, consistent with spin 1/2 scenario. Given the valance of Sb is -3, the valance of Cr is +(3-δ/6), δ represent the charge transfer of single Cs atom to CrSb layer. The magnetic moment of Cr suggests the filling is close to d^3 at a low spin state of crystal tetrahedral field (1.73 μ_B). Using the extrapolated high-temperature magnetic susceptibility, we calculated the Sommerfeld-Wilson ratio of the bulk to be 3.4, indicating the existence of short-range magnetic interactions.

The fitted Neel temperature is 750 K, much higher than T_F, suggesting strong magnetic frustration of $CsCr_6Sb_6$ prevent the magnetic ordered state in the bulk sample.

Supplementary Note 3: Measurement of correlation strength

The correlation strength U/W, characterized by the mass renormalization m/m_0, can be quantified by several parameters captured by experiments. Most common are the Sommerfeld coefficient γ of the electronic specific heat C and A coefficient of the electrical resistivity ρ. m/m_0 can be directly determined from γ and the carrier concentration n. The specific of free electrons can be described as

$$C = \frac{\pi^2}{3} N(E_F) {k_B}^2 \quad (1)$$

Here $N(E_F)$is DOS of free electron at E_F, which is

$$N(E_F) = \frac{V}{4\pi^3} \frac{m}{\hbar^2 k_F} 4\pi {k_F}^2 \quad (2)$$

Where k_F is Fermi wave vector. It can be related to n as

$$k_F = 2\left(\frac{3}{8\pi}\right)^{1/3} n^{1/3} \quad (3)$$

Using the carrier density extracted from Hall measurements at 1.8 K, n=7.5∗10^{19}cm^{-3}, and the unit cell volume V=306.6 Å^3/f.u.. We deduce a free electronic Sommerfeld coefficient γ_0=1.26 mJ/mol/K^2. The ratio between experimental and the calculated value equal to m/m_0, which is

$$\frac{\gamma_{exp}}{\gamma_0} = 60 \quad (4)$$

According to the Kadowaki-Woods scaling A/γ^2=10 $\mu\Omega$ cm mol^2 K^2 J^{-2} (ref. 1), γ and A measure the same quantity, m/m_0. Spectroscopy offers another way to measure the correlation strength. The bands observed in ARPES can be fitted with a Schrodinger-like dispersion $\varepsilon=\hbar^2k^2/(2m)$ to extract m/m_0. This method can be extended to Dirac-like dispersion $\varepsilon=\hbar vk$, in which the measured Dira velocity v can be renormalized with a non-interacting v.

Supplementary Note 4: Symmetrization and anti-symmetrization of the magneto-transport data

The geometry of typical few-layer $CsCr_6Sb_6$ samples is usually irregular and random, leading to the mixing of *Rxx* and *Rxy* signals in the standard six-terminal measurements. The raw magneto-transport data are shown in Supplementary Fig. 11. Since R_{xx} is symmetric with respect to the polarity of the magnetic field $\mu_0 H$, while R_{xy} is antisymmetric. We apply standard symmetrization and anti-symmetrization procedures to isolate the two components, resulting in the data shown in the main figures. The symmetrization procedure for *Rxx* is as follows:

$$R_{xx}^{\uparrow}(\mu_0 H) = \frac{1}{2}\left[R_{xx,raw}^{\uparrow}(\mu_0 H) + R_{xx,raw}^{\downarrow}(-\mu_0 H)\right] \quad (5)$$

$$R_{xx}^{\downarrow}(\mu_0 H) = \frac{1}{2}\left[R_{xx,raw}^{\downarrow}(\mu_0 H) + R_{xx,raw}^{\uparrow}(-\mu_0 H)\right] \quad (6)$$

$$R_{xx}^{\uparrow}(-\mu_0 H) = R_{xx}^{\downarrow}(\mu_0 H) \quad (7)$$

$$R_{xx}^{\downarrow}(-\mu_0 H) = R_{xx}^{\uparrow}(\mu_0 H) \quad (8)$$

The anti-symmetrization procedure for R_{xy} is as follows:

$$R_{xy}^{\uparrow}(\mu_0 H) = \frac{1}{2}\left[R_{xy,raw}^{\uparrow}(\mu_0 H) - R_{xy,raw}^{\downarrow}(-\mu_0 H)\right] \quad (9)$$

$$R_{xy}^{\downarrow}(\mu_0 H) = \frac{1}{2}\left[R_{xy,raw}^{\downarrow}(\mu_0 H) - R_{xy,raw}^{\uparrow}(-\mu_0 H)\right] \quad (10)$$

$$R_{xy}^{\uparrow}(-\mu_0 H) = -R_{xy}^{\downarrow}(\mu_0 H) \quad (11)$$

$$R_{xy}^{\downarrow}(-\mu_0 H) = -R_{xy}^{\uparrow}(\mu_0 H) \quad (12)$$

Here we set $\mu_0 H>0$. The subscript raw denotes raw data, and the superscripts ↑and ↓ indicate the direction of the sweeping field.

Supplementary Note 5: Electronic structure calculations

Electronic structure calculations are carried out using density functional theory with the projector augmented wave method, as implemented in the Vienna Ab initio Simulation Package (VASP) [2,3]. A plane-wave cutoff energy of 265.7 eV was used. We employed the generalized gradient approximation[4] (GGA) and projector augmented-wave method[5], explicitly including nine valence electrons for Cs ($5s^2 5p^6 6s^1$), twelve valence electrons for Cr ($3s^2 3p^6 4s^1 3d^5$) and five valence electrons for Sb ($5s^2 5p^3$). Here we use ab-initio relaxed crystal structure which is relaxed with a convergence criterion such that the forces on the atoms are less than 3 meV/Å. The effective Coulomb interaction parameter was evaluated using constrained random phase approximations (CRPA) based on the maximally localized Wannier function. The cut-off energy of response function is set to 177.1 eV, and 470 empty states were used to evaluate the RPA response function. The Coulomb integrals were projected on the target Wannier basis and then the effective Hubbard interaction U is obtained.

The projected band structures near the Fermi energy, as shown in Supplementary Fig. 12. The d_{xz} and d_{yz} orbitals have lower energy and contribute primarily to the flat bands at Γ-L and Z-M_2. In contrast, the d_{x2-y2} and d_{xy} orbitals have higher energy and contribute mainly to the dispersive parts at M_2-H_2 and L-S_0-Γ. Hence, the half-filled d_{xz} and d_{yz} orbitals provide localized electrons and the d_{x2-y2} and d_{xy} orbitals provide itinerant electrons, forming a Kondo lattice. The discrepancies between the ARPES data and the ab initio calculations arise from the strong correlation effects, which are challenging to capture with standard ab initio methods.

One-shot single-site DFT+DMFT calculations are performed for the paramagnetic phases of $CsCr_6Sb_6$. We construct a two-orbital model of $CsCr_6Sb_6$ in which d_{xy} and d_{x2-y2} orbital are regarded as the same orbital due to the degeneracy so as d_{xz} and d_{yz} orbitals. The local orbitals are constructed using maximally localized Wannier function implemented in Wannier90 code[6]. Electron states of Cr d orbitals within an energy window from -1 to 0.5 eV is included in the wannierization. The local axis of Cr d orbitals is adjusted to keep the -3m site symmetry. All orbitals are considered correlated and double counting in fully localized limit form is chosen. The continuous time quantum Monte Carlo is used as impurity solver, as implemented in TRIQS-cthyb package[7,8]. The self-energy on real frequency is obtained by the analytical continuation method of Padé appeoximation.

Supplementary Table 1 Crystal data of $CsCr_6Sb_6$ at different temperature.

Formula	$CsCr_6Sb_6$	$CsCr_6Sb_6$
Temperature (K)	300 K	40 K
crystal system space	Trigonal	Trigonal
group	$R\bar{3}m$(166)	$R\bar{3}m$(166)
a (Å)	5.5462	5.5482
b (Å)	5.5462	5.5482
c (Å)	34.5280	34.3100
α (°)	90	90
β (°)	90	90
γ (°)	120	120
volume ($Å^3$)	919.7993	914.6514
Z	3	3
μ (mm^{-1})	20.932	21.050
F(000)	1509.9	1515
radiation	Mo K_α(λ=0.71073)	Mo K_α(λ=0.71073)
Reflections collected	335	277
Goodness-of-fit on F^2	1.0179	1.124

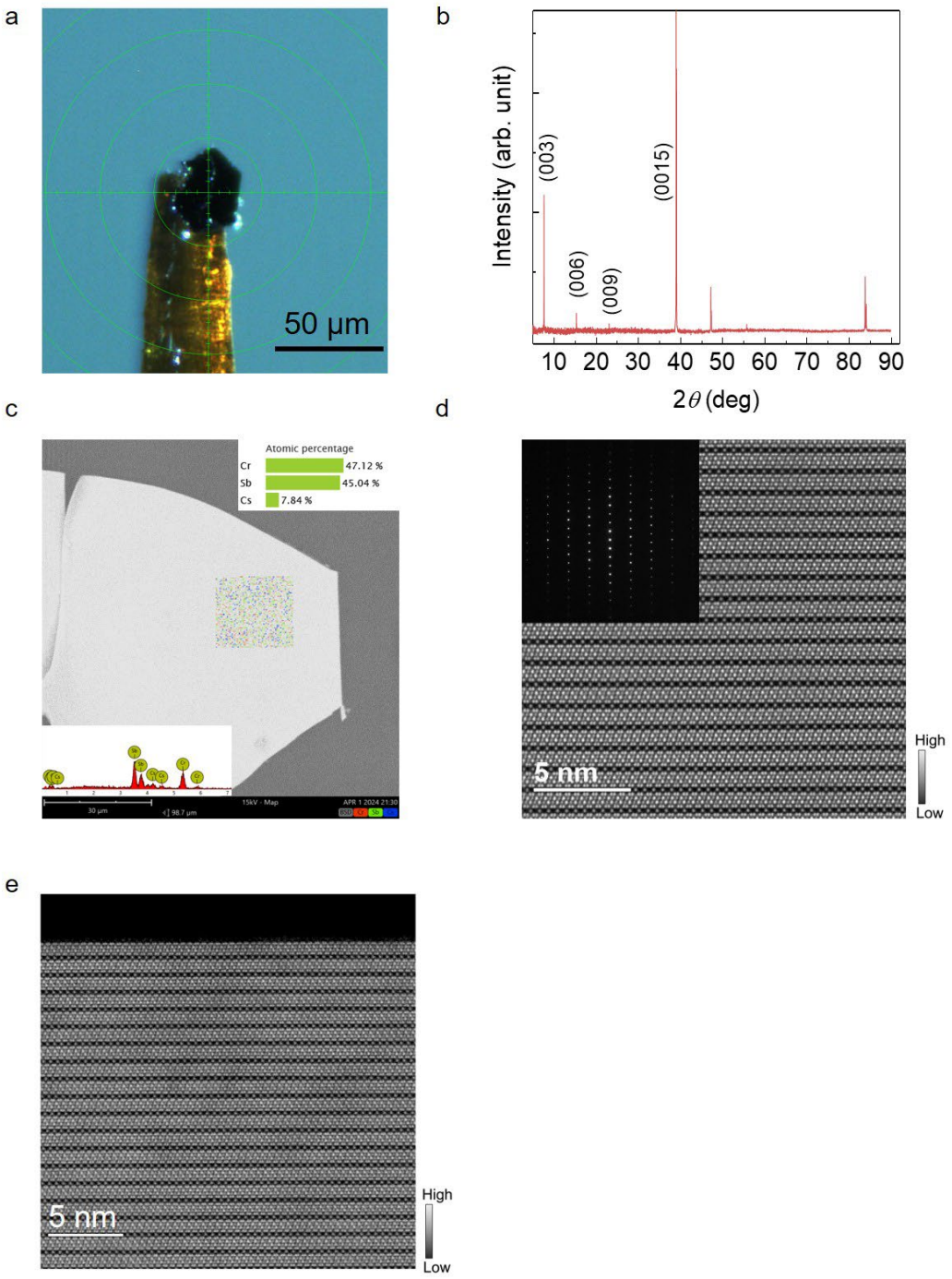

Supplementary Fig. 1 | Characterization of bulk $CsCr_6Sb_6$. a Optical image of the crystal measured in the single crystalline X-ray diffraction. **b** XRD spectra of $CsCr_6Sb_6$ on (001) surface. **c** Surface scan of energy dispersive spectroscopy. Red, green and blue spots are elements mapping of Cr, Sb and Cs, respectively. **d** Extended view of the Atomic-resolution image of $CsCr_6Sb_6$. **e** Cross-sectional image on the edge of a slab sample. Only the surface Cs layer is lost, while all inner Cs layers remain well preserved.

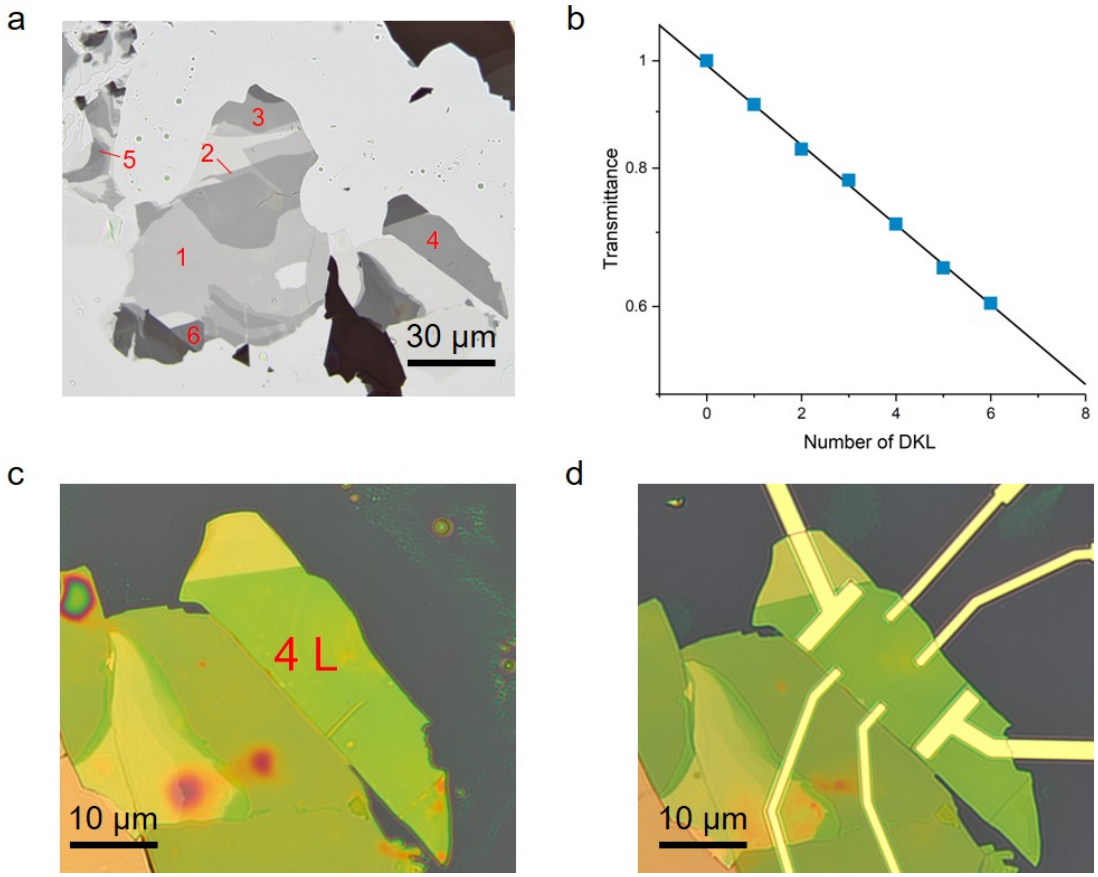

Supplementary Fig. 2 | Fabrication and characterization of few-layer samples. a Optical image of few-layer samples assisted by Al_2O_3 in a transparent mode. Number of layers of the samples can be determined by optical transmittance and marked use red characters. **b** Transmittance extracted from blue channel of the samples in (**a**). Black line is the fitting of Beer-Lambert Law. **c** Optical image of the 4 L flake on a silicon substrate. **d** Fabricated device with electrodes.

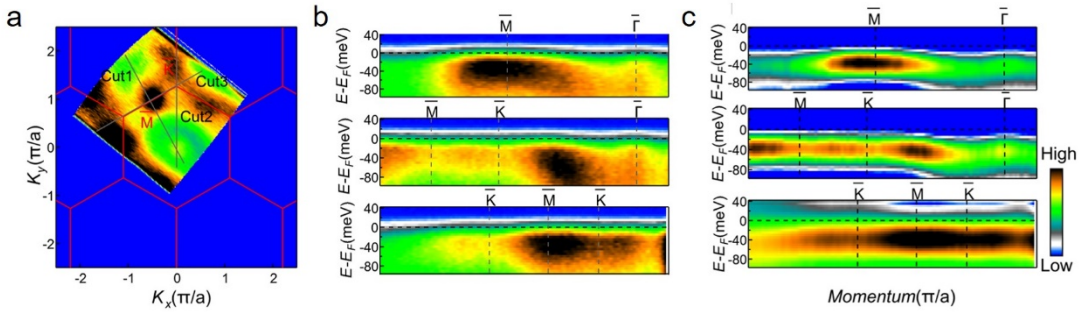

Supplementary Fig. 3 | EDC Second derivative of the flat bands. a Fermi surface mapping of $CsCr_6Sb_6$ measured at a 15 K. **b** Detailed band structures measured along the three high symmetry directions. **c** EDC second derivative photoemission spectra corresponding to the original images in (**b**) to show the band structure clearly.

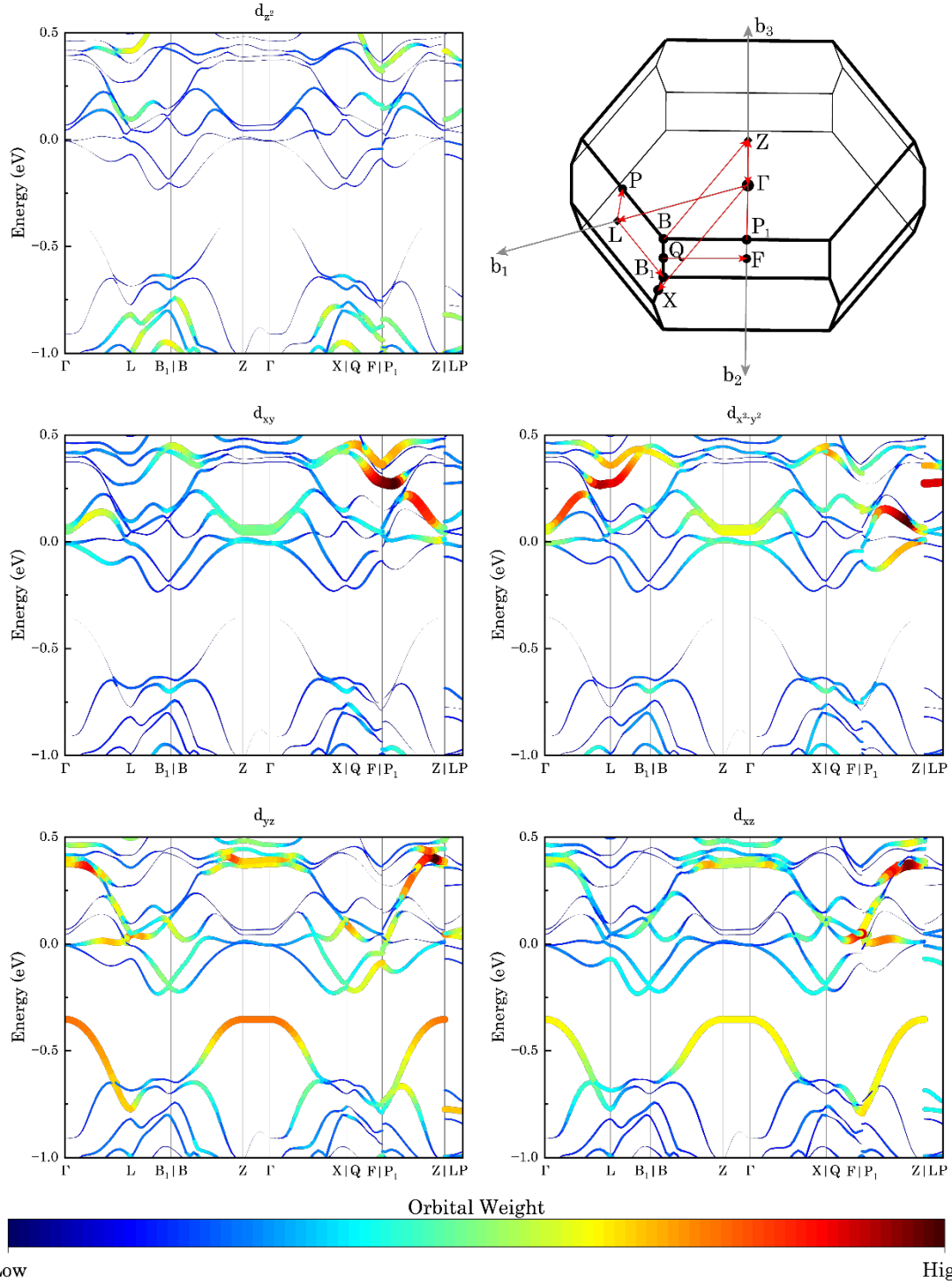

Supplementary Fig. 4 | Projected band structure and wavefunction. Top right panel is the Brillouin zone and the high-symmetry path. Other panels are band structure of $CsCr_6Sb_6$. The color scale represents the spectra weight of Cr' *d* orbitals.

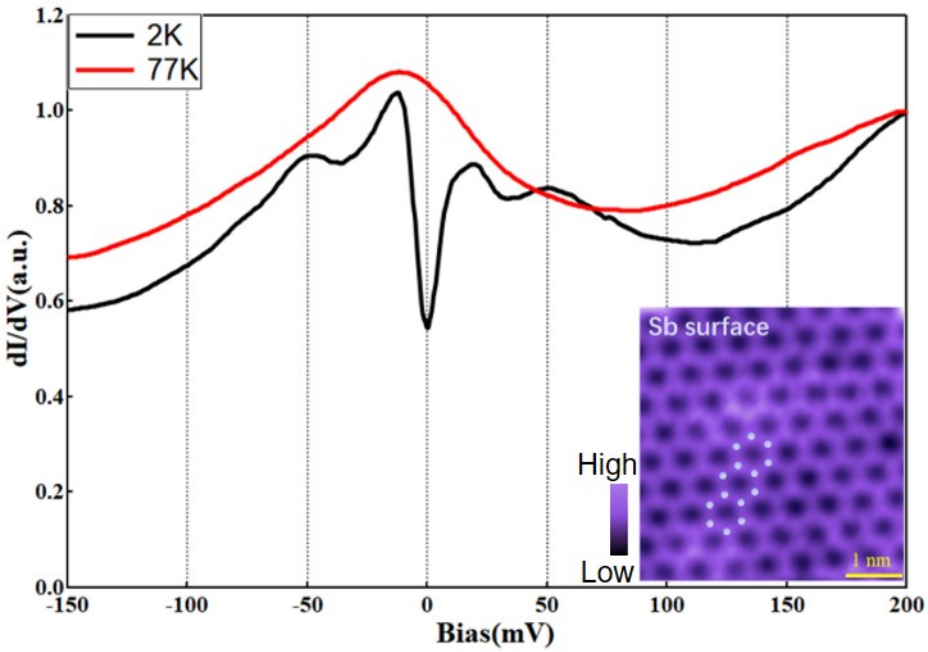

Supplementary Fig. 5 | Scanning tunneling microscopy and spectroscopy measurements of $CsCr_6Sb_6$. The black and red curves represent the dI/dV spectra acquired at 2 K and 77 K, respectively. The inset shows the topography of the cleaved Sb surface, with the honeycomb Sb lattice overlaid for reference.

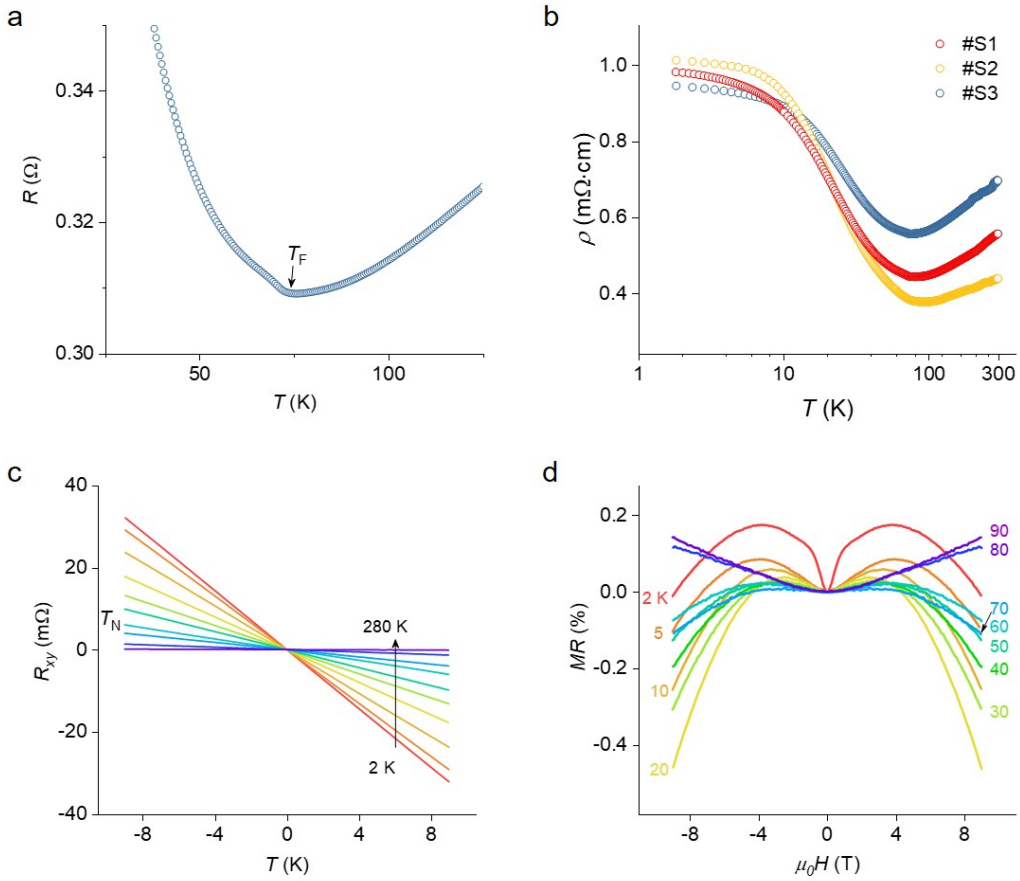

Supplementary Fig. 6 | Electrical transport data of bulk $CsCr_6Sb_6$. a Resistivity kink results from RKKY interaction. **b** Resistivity of $CsCr_6Sb_6$ acquired from three different batches of sample, indicating the intrinsic large normal-state resistivity. **c** R_{xy} at various temperature, the slope at high field change sign at T_F. **d** *MR* of bulk sample at various temperatures.

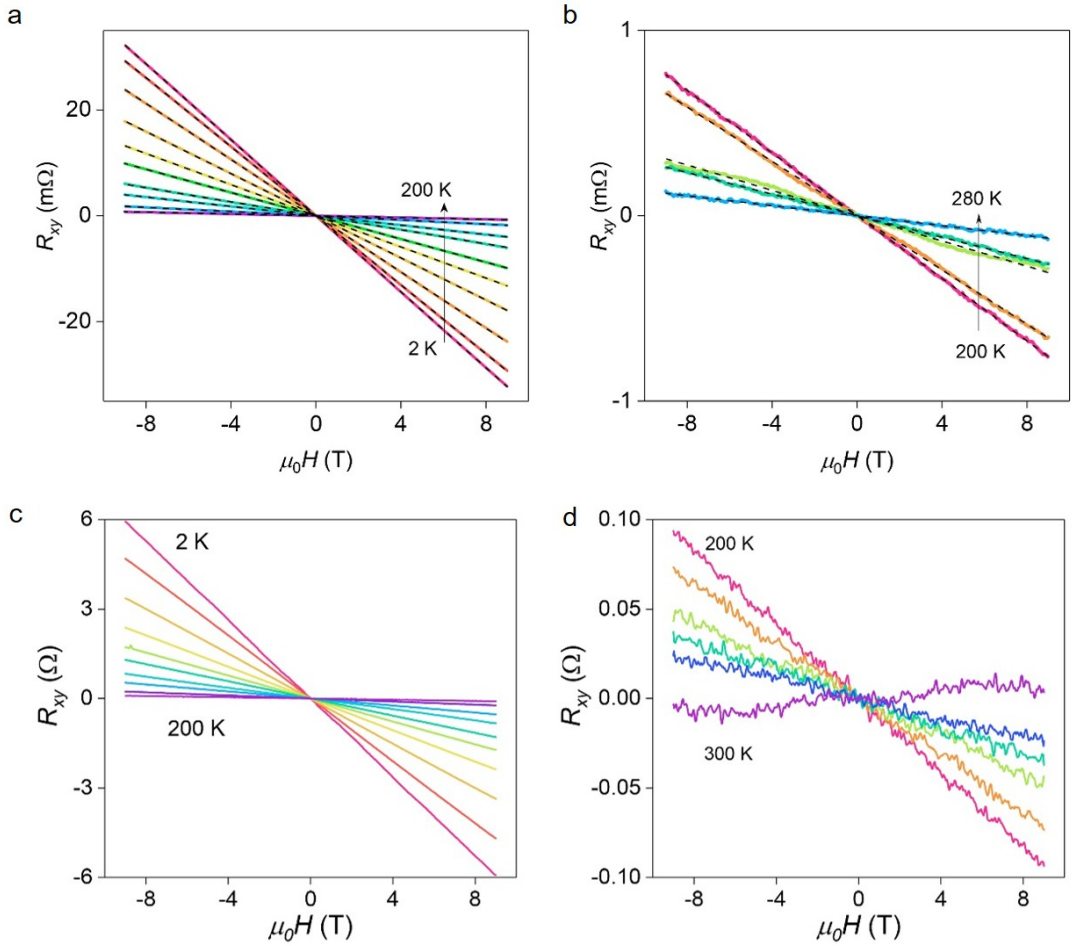

Supplementary Fig. 7 | a and **b** R_{xy} of the bulk sample in main text, it can be used to fit R_H which is independent on H. Dashed lines are linear fitting of R_{xy}. **c** and **d** R_{xy} of a 50 nm sample. It deviate from linearity at high temperature, suggesting multi-type carrier in $CsCr_6Sb_6$.

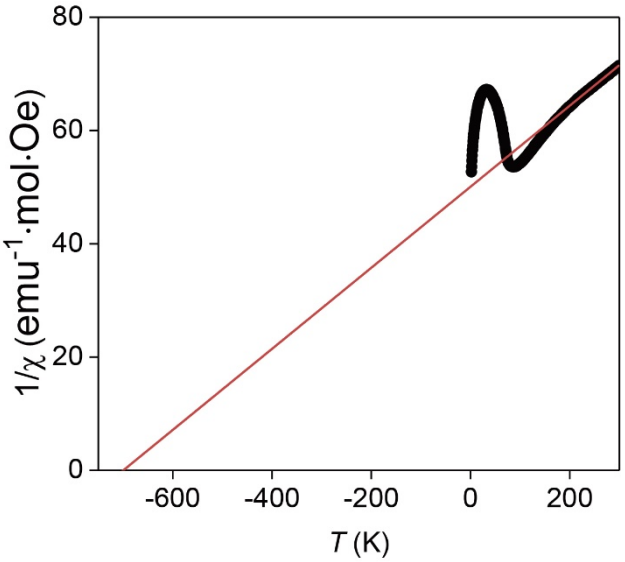

Supplementary Fig. 8 | Curie-Weiss fitting of the magnetic susceptibility. Extracted magnetic moment is 1.76 μ_B per Cr. The fitted Neel temperature is much higher than T_F, suggesting the strong frustration.

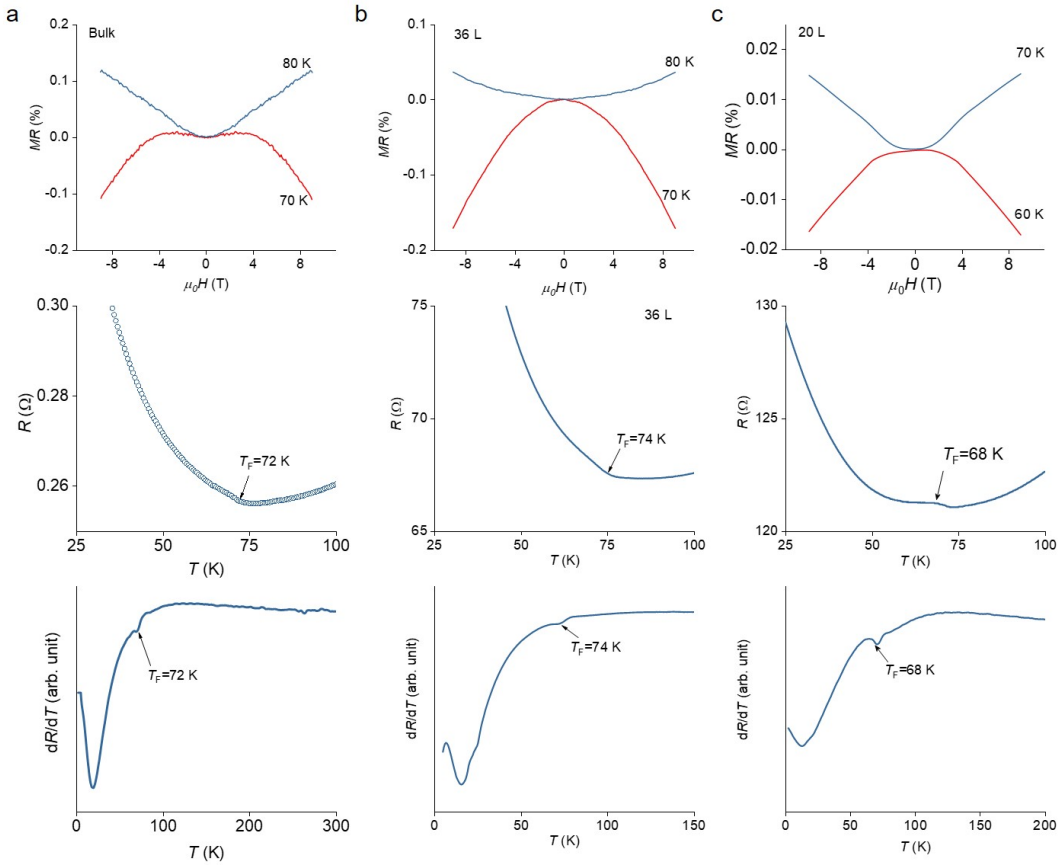

Supplementary Fig. 9 | Determination of T_F. Four representative samples: bulk (**a**) and a 36L thick flake (**b**) with frustrated magnetization, a 20L thin flake (**c**). The upper, middle and lower panels are the raw data of *MR*, resistance and d*R*/d*T*, respectively.

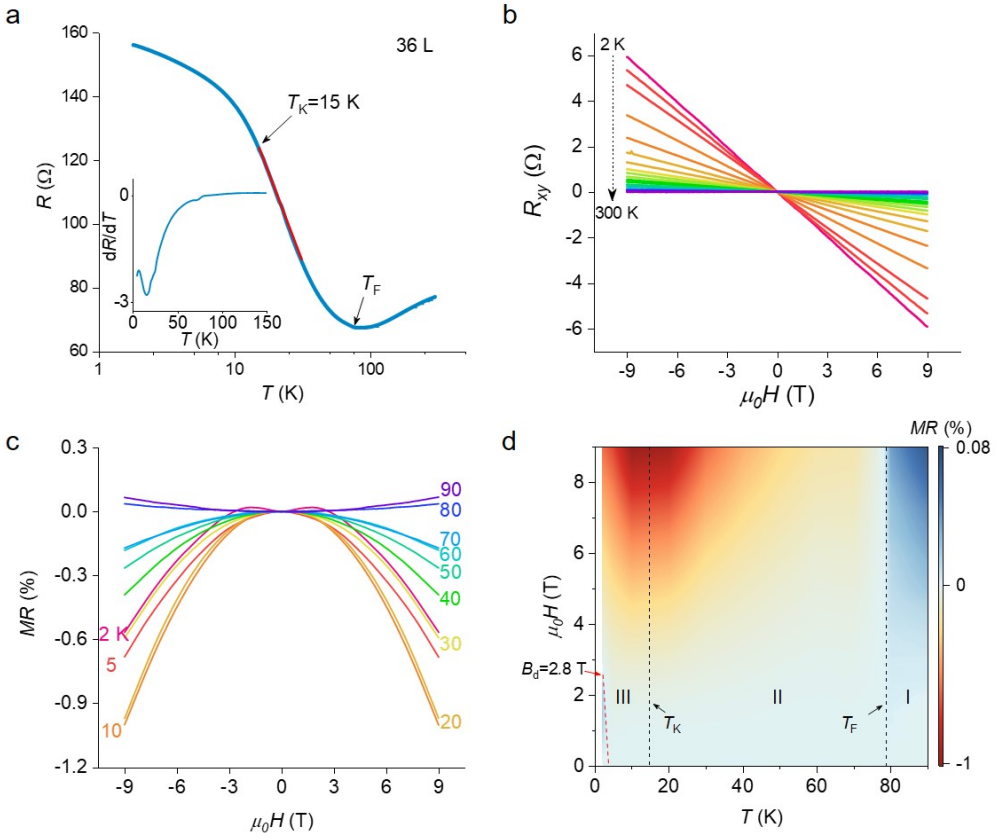

Supplementary Fig. 10 | Electrical transport data of a 36 L flake sample. a temperature dependent resistance of 36 L sample. T_K and T_F are defined as that of the bulk. Inset is the first derivate of resistivity. **b** R_{xy} at temperature from 2 to 300 K. The hall resistivity is linear to magnetic field, same as that in bulk. **c** *MR* at various temperatures, the slope at high field change sign between 70 and 80 K. **d** the contour plot of *MR*, T_K represent the maximum of the negative *MR* at 15 K. The critical magnetic field crossover from positive to negative *MR* at 2 K is 2.8 T, much lower than that in bulk.

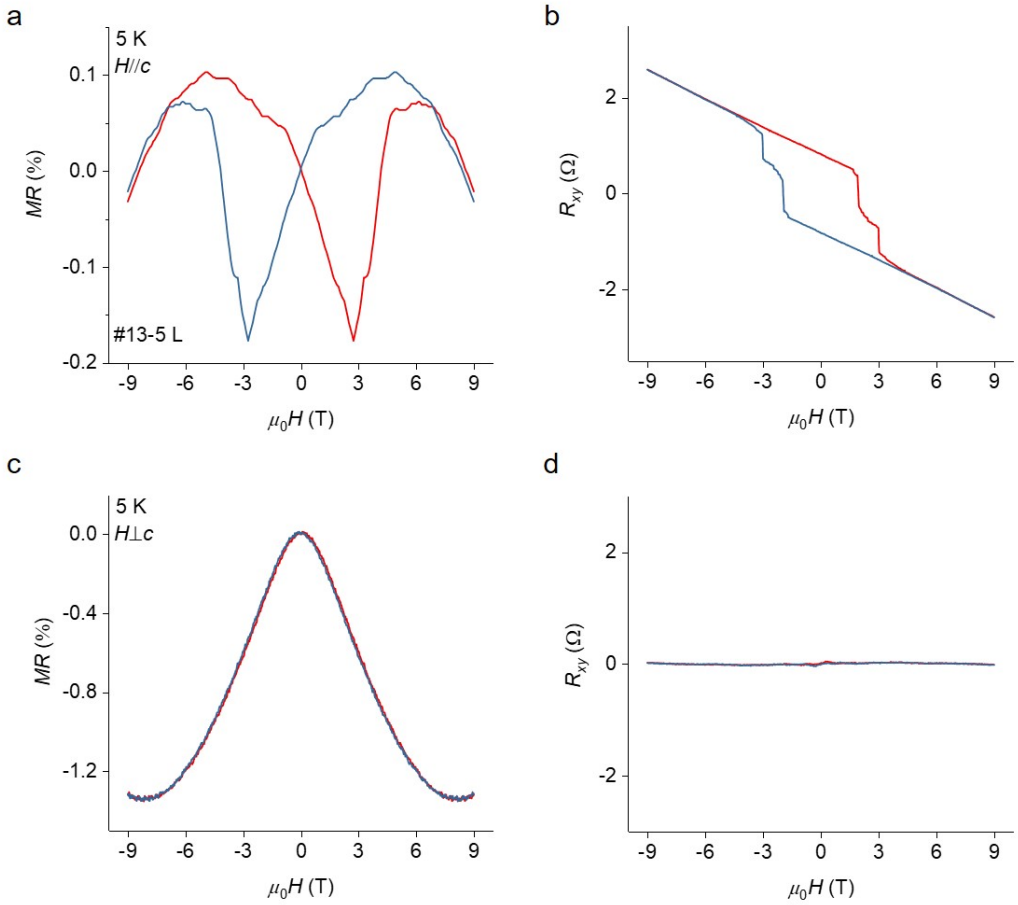

Supplementary Fig. 11 | Easy magnetization axis of the few-layer samples. a, **b** *MR* and R_{xy} of 5 L sample with the magnetic field along the *c*-axis at 5 K. Resistance jump at 2 and 3 T can be clearly seen. Red and blue curves represent up and down sweep of magnetic field, respectively. **c**, **d** Same measurements as (**a**) and (**b**) but with the magnetic field within the ab-plane. The jumps are absent below 9 T, indicating an out-of-plane easy axis. Red and blue curves represent up and down sweep of magnetic field, respectively.

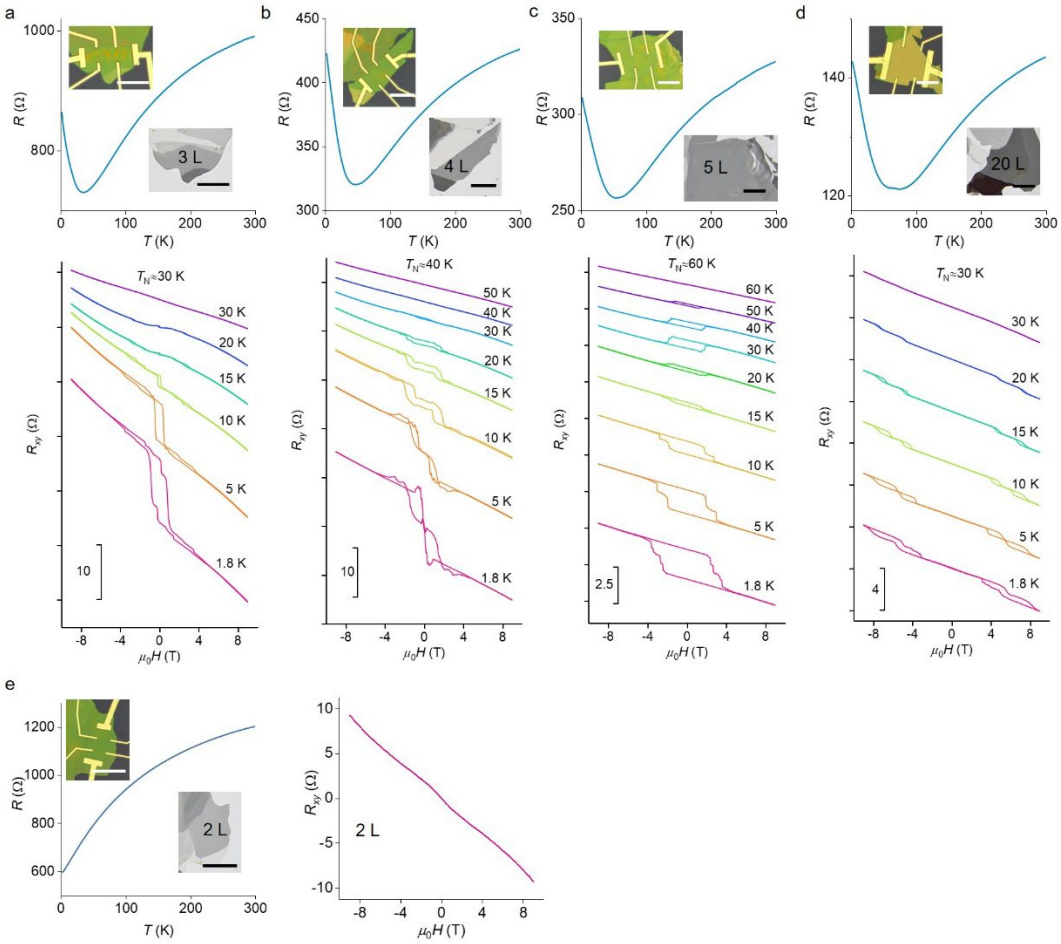

Supplementary Fig. 12 | Electrical data of various thin flakes and the determination of T_N. a-e Upper panels are the raw data of the resistivity with different sample thickness. Left insets are the optical image of the fabricated devices and the right insets are transparent mode images that used to determine the sample thickness. Lower panel are temperature dependent of R_{xy}. Anomalous Hall resistance can be seen at low temperature. T_N is defined at the critical temperatures when the hysteresis emerges. Scale bar in all optical images are 10 μm.

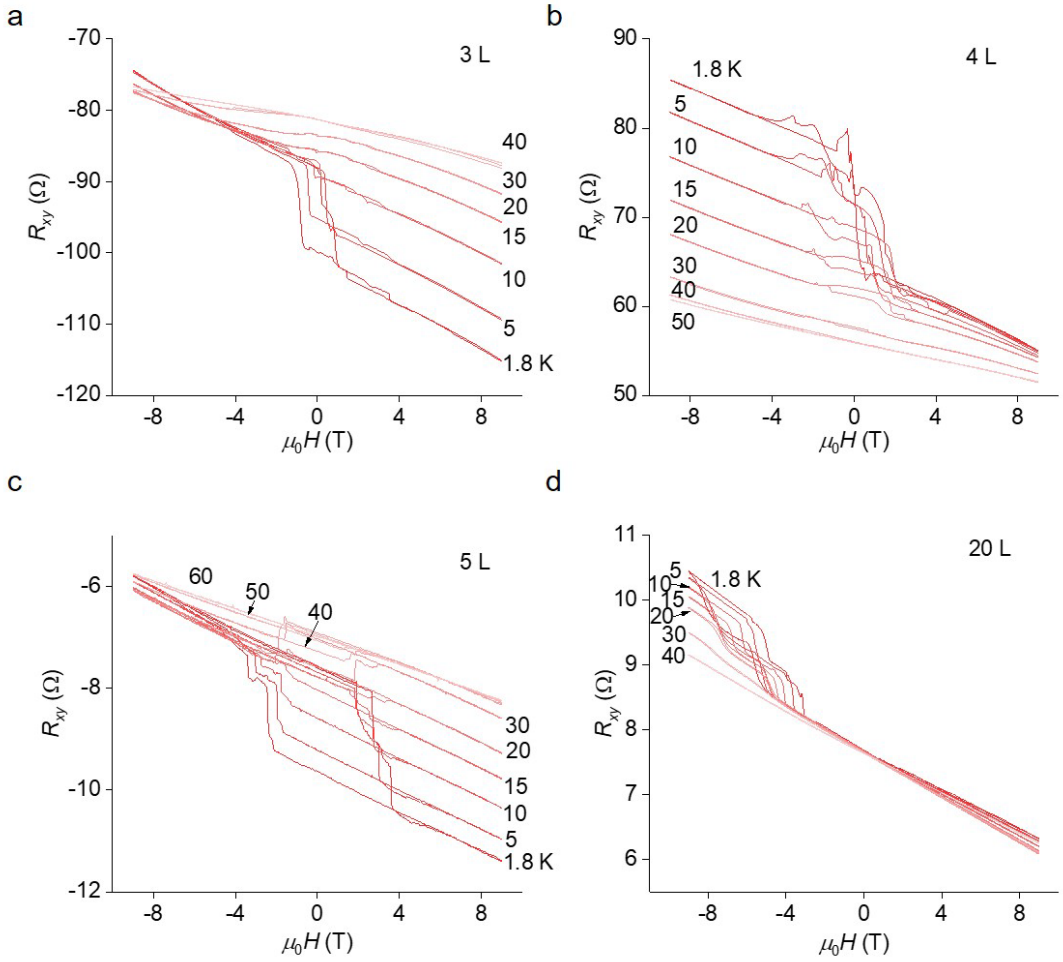

Supplementary Fig. 13 | Raw Hall data of few-layer samples. a-d Raw R_{xy} of samples in main text at various temperature. The Hall data are asymmetric because of irregular geometry of the samples.

References

1. Kadowaki, K. & Woods, S. B. Universal relationship of the resistivity and specific heat in heavy-fermion compounds. *Solid State Commun.* **58**, 507–509 (1986).
2. G. Kresse and J. Furthmüller Efficient iterative schemes for ab initio total-energy calculations using a plane-wave basis set. *Phys*. *Rev*. *B* **54**, 11169 (1996).
3. G. Kresse and J. Furthmüller Efficiency of ab-initio total energy calculations for metals and semiconductors using a plane-wave basis set. *Comput*. *Mat*. *Sci*. **6**, 15 (1996).
4. J. P. Perdew, K. Burke, and M. Ernzerhof Generalized Gradient Approximation Made Simple. *Phys*. *Rev*. *Lett*. **77**, 3865 (1996).
5. P. E. Blochl Projector augmented-wave method. *Phys*. *Rev*. *B* **50**, 17953 (1994).
6. Giovanni Pizzi et al. Wannier90 as a community code: new features and applications. *J*. *Phys*. *Cond*. *Matt*. **32**, 165902 (2020).
7. Olivier Parcollet et al. TRIQS: A toolbox for research on interacting quantum systems. *Comp*. *Phys*. *Comm*. **196**, 398-415 (2015).
8. Priyanka Seth et al. TRIQS/CTHYB: A continuous-time quantum Monte Carlo hybridisation expansion solver for quantum impurity problems. *Comp*. *Phys*. *Comm*. **200**, 274–284 (2016).